Available online at www.sciencedirect.com
ScienceDirect
Trans. Nonferrous Met. Soc. China 32(2022) 3036−3050
Transactions of Nonferrous Metals Society of China
www.tnmsc.cn

Determination of dynamic mode I fracture toughness of rock at ambient high temperatures using notched semi-circular bend method

You WU, Tu-bing YIN, Xi-ling LIU, Xiao-song TAN, Zheng YANG, Qiang LI

School of Resources and Safety Engineering, Central South University, Changsha 410083, China

Received 16 August 2021; accepted 25 February 2022

Abstract: To investigate the influence of loading rate and high temperature on the dynamic fracture toughness of rock, dynamic fracture tests were carried out on notched semi-circular bend specimens under four temperature conditions based on the split Hopkinson pressure bar system. Experimental and analytical methods were applied to investigating the effect of temperature gradient on the stress waves. A high-speed camera was used to check the fracture characteristics of the specimens. The results demonstrate that the temperature gradient on the bars will not significantly distort the shape of the stress wave. The dynamic force balance is achieved even when the specimens are at a temperature of 400 °C. The dynamic fracture toughness linearly develops with the increase of loading rate within the temperature range of 25−400 °C, and high temperature has a strengthening effect on the dynamic fracture toughness.

Key words: ambient high-temperature condition; dynamic fracture toughness; notched semi-circular bend specimen; split Hopkinson pressure bar; Fujian granite

1 Introduction

Studying the dynamic properties of rock materials at ambient high temperatures has drawn much attention in the rock mechanics community because rocks and rock structures are vulnerable to the coupling effects of high temperature and dynamic disturbance in civil and underground engineering, such as the fire and explosion accident in stone buildings, rock tunnels and underground mines [1−6], and the exploitation of geothermal and oil−gas resources [7,8].

Up to now, the dynamic compressive [9−15] and dynamic tensile [16,17] properties of rocks at ambient high temperatures have been widely studied based on the split Hopkinson pressure bar (SHPB) system. However, the dynamic fracture properties of rock materials at ambient high temperatures remain far from being understood [18,19]. ZHANG et al [18] tested the dynamic fracture toughness of Fangshan gabbro and Fangshan marble at high temperatures (100−330 °C) by using short rod (SR) specimens. YIN et al [19] estimated the dynamic fracture toughness of Changsha granite at different high temperatures (20−400 °C) based on the discrete element method (DEM). However, their results are still quite limited to cover all situations. For example, the crack propagation process of the SR specimen is hard to be experimentally observed, because the SR specimen is based on the chevron crack. While for YIN et al [19], although they successfully conducted the dynamic fracture study based on the DEM, careful parameter calibration, which is usually very hard in most situations, is inevitable in a numerical study for the reliability of numerical results. Besides, physical mechanisms should usually be investigated through indoor experiments, which are the most reliable way to obtain the physical properties of rock materials.

Corresponding author: Xi-ling LIU, Tel: +86-731-88879612, E-mail: lxlenglish@163.com
DOI: 10.1016/S1003-6326(22)66001-1

Moreover, there is a lack of available technology for carrying out the dynamic fracture test at ambient high temperatures. LIU and XU [9,10] devised a test method to study the dynamic compressive properties of rocks at ambient high temperatures. Their method comprises four test procedures: (1) heat the specimen in an electric furnace; (2) transfer the specimen to a heating furnace on the SHPB system to compensate for the heat loss of the specimen; (3) assemble the SHPB system rapidly to sandwich the specimen between the incident and transmitted bars; (4) load the specimen before the heat influences the mechanical properties of the steel bars. However, a review of the literature [20−30] indicates that the specimens used for the dynamic fracture tests are usually complex in geometry, which makes the method difficult to conduct.

YIN et al [16] presented a new method to test the dynamic properties of rocks at ambient high temperatures. The method allows the specimen to be heated with the bars and avoids complex test procedures. However, due to high temperature, the basic properties, such as elastic modulus, of the bar will be changed. And, the waveform and propagation of the stress wave will be affected to some extent. In this work, the method was adopted to test the dynamic mode I fracture toughness of granite at ambient high temperatures using the notched semi-circular bend (NSCB) specimens based on the SHPB system. The effect of high-temperature gradient on the propagation of the stress wave was analyzed and the modified stress waves were used to calculate the dynamic fracture toughness of the rock at ambient high temperatures.

2 Experimental

2.1 Specimen description

The granite, which is well-known as Fujian G654 granite, used in this study was collected from Changtai County, Zhangzhou City, Fujian Province, China. Significantly, the Zhangzhou basin is rich in hot dry rock and has a high potential geothermal developing value [31]. The mechanical properties of the granite in natural conditions are shown in Table 1. The granite has a density of 2795 kg/m^3, P-wave velocity of 5069 m/s, uniaxial compressive strength of 174.78 MPa, mode I fracture toughness of 1.349 MPa·m$^{0.5}$, and mode II fracture toughness of 3.45 MPa·m$^{0.5}$ [32,33]. This granite is usually regarded as an isotropic material and is widely applied to the mechanical tests for different purposes [32−34].

Figure 1 shows the photographs and the configuration of the prepared NSCB specimens. The manufacturing of the specimens rigidly followed the recommended methods of the international society for the rock mechanics (ISRM) [23,35]. The radius (R) of the fabricated specimens is 25 mm, the thickness (B) is 25 mm, the crack length (a) is 8.33 mm, the crack width (t) is 1 mm, and the span of the supporters (S) is 34 mm.

Table 1 Mechanical properties of granite in natural conditions [32,33]

ρ/(kg·m^{-3})	P_v/(m·s^{-1})	σ_t/MPa	σ_c/MPa	K_{IC}/(MPa·m$^{0.5}$)	K_{IIC}/(MPa·m$^{0.5}$)	E/GPa	μ
2795	5069	11.63	174.78	1.349	3.45	28.94	0.2

ρ: Density; P_v: Longitudinal wave velocity; σ_t: Tensile strength; σ_c: Uniaxial compressive strength; K_{IC}: Mode I fracture toughness; K_{IIC}: Mode II fracture toughness; E: Elastic modulus; μ: Poisson's ratio

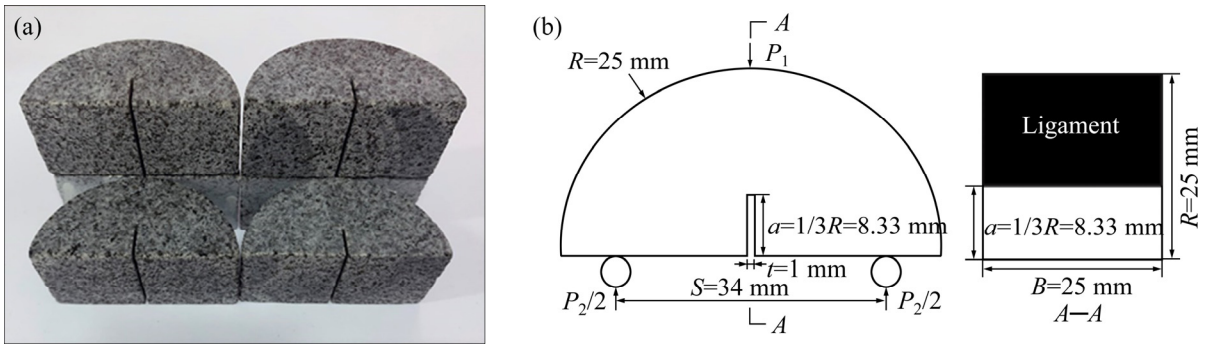

Fig. 1 Photograph of prepared NSCB specimens (a), and configuration of NSCB specimens (b)

2.2 Experimental setup

An SHPB system (improved by LI et al [36]) was used for carrying out the dynamic fracture tests. The SHPB system is located at the School of Resources and Safety Engineering, Central South University, China. A schematic diagram of the SHPB system is shown in Fig. 2. The SHPB system contains a gas gun, a cone-shaped striker, an incident bar, a transmitted bar, an absorption bar, a damper, and a heating box. The length of the incident bar is 2 m and the length of the transmitted bar is 1.5 m. All of the bars are 50 mm in diameter and made of Cr40 alloy steel. At a normal temperature (25 °C), the density and elastic modulus of the alloy are 7810 kg/m^3 and 211 GPa, respectively. Strain gauges were employed in the middle of the incident and transmitted bar to collect the strain signals with an acquisition rate of 10^6 samples per second. A high-speed camera was synchronously coupled with the SHPB system to catch the failure characteristics of the NSCB specimen with a frame rate of 100000 frame/s and a resolution of 192×192.

For a dynamic fracture test, an NSCB specimen was sandwiched between the incident and transmitted bars. The electric furnace was then turned on to heat the specimen with a heating rate of 10 °C/min [9,16]. When the designated temperature (100, 200, and 400 °C) was reached, the temperature was kept at this value for 1 h to ensure that the whole specimen attained the same temperature field. The electric furnace allowed the incident and transmitted bars to pass through the furnace body, and the specimen and bars can be heated together. After the heating procedures, a con-shaped striker was launched from the gas gun, generating a half-sine incident wave as the elastic collision of the striker and the incident bars. The incident wave propagated along the incident bar, and when it came into contact with the specimen, the reflected and transmitted waves would be generated accordingly. When the fracture tests were carried out at the normal temperature (25 °C), the forces (P) on both sides of the specimen can be written as [23]

$$P_1=AE(\varepsilon_i+\varepsilon_r)=A(\sigma_i+\sigma_r),\ P_2=AE\varepsilon_t=A\sigma_t \quad (1)$$

where A is the cross-sectional area of the steel bars; E is the elastic modulus of the steel bars; ε_i, ε_r and ε_t are the incident, reflected, and transmitted strain signals, respectively; σ_i, σ_r and σ_t are the incident, reflected, and transmitted stress signals, respectively.

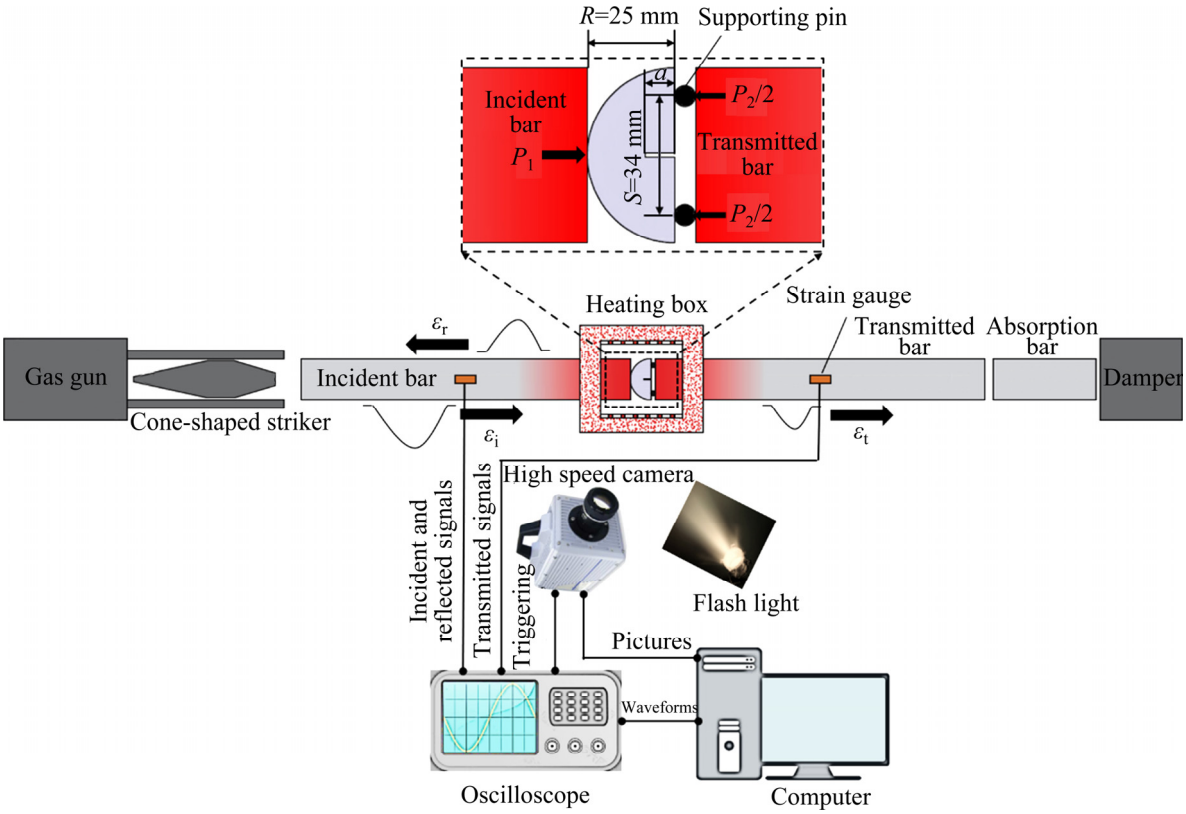

Fig. 2 Schematic diagram for SHPB system

3 Data processing

3.1 Effect of temperature gradient on stress wave

It should be noted that when the bars were heated with the NSCB specimen, the elastic modulus of the bars will be changed due to high temperature. Therefore, Eq. (1) cannot be directly used for calculating the forces on the specimen. The temperature distributions on the incident and transmitted bars were measured and shown in Fig. 3 when the furnace was heated to 100, 200, and 400 °C, respectively, and kept at the temperature for 1 h. The bars maintained the highest temperature in the furnace chamber, but when moving away from the furnace chamber, the temperature of the bars decreased exponentially. In the middle part of the steel bars, the temperature was very close to normal temperature. According to the Practical Manual for Engineering Materials [37], the elastic modulus for Cr40 alloy steel at different temperatures is shown in Table 2. The elastic modulus of the steel bars is 211 GPa when the steel is at 25 °C. However, it decreases to 186 GPa when the temperature increases to 400 °C. Therefore, because there is a temperature gradient on the incident and transmitted bars, the forces calculated based on Eq. (1) must not be the true forces on the specimen.

Before the dynamic fracture tests, the law of temperature gradient on the stress waves should be investigated so as to derive the true forces on the specimen. However, it is very hard to directly measure the stress waves on the steel bars when the bars are at high temperatures. Therefore, an indirect method was used herein to test the influence of temperature gradient on the stress wave. As shown in Fig. 4, the incident bar is slightly separated from the transmitted bar, which allows the reflection of the incident wave at the right free surface. Figure 5(a) presents the voltage signals obtained by the strain gauge on the incident bar when the SHPB device works at a normal temperature (25 °C) and the air pressure is 0.4 MPa. It can be seen from Fig. 5(a) that the stress wave signals for the three independent impacts (Specimens 25-1, 25-2, and 25-3) are similar, which suggests the repeatability of the test results. Figure 5(b) shows the comparison between the incident wave and the reflected wave for 25-1, where the time-zero of the incident and reflected waves is shifted into the points when the waves begin to change. Based on the principle of one-dimensional stress wave theory, the amplitude reflected wave will be entirely equal to the incident wave. However, from Fig. 5(b), the amplitude of the incident wave is slightly lower than that of the reflected wave, which can be mainly attributed to the natural attenuation of the stress wave.

The same procedures were carried out when the furnace was heated to 100, 200, and 400 °C, respectively. The comparison between the incident and reflected waves is presented in Fig. 6. Intuitively, the difference between the incident and reflected waves will be more and more pronounced with the increase in temperature. However, according to Fig. 6, the reflected signals are seemed to be less dependent on temperature and there is no obvious difference between the incident and reflected waves at different temperatures.

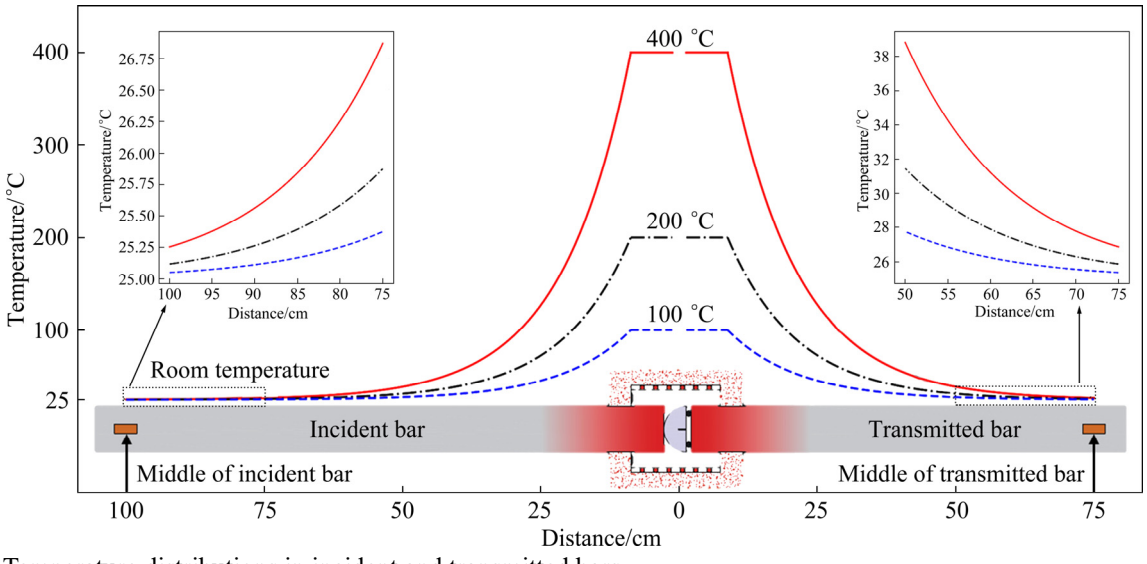

Fig. 3 Temperature distributions in incident and transmitted bars

Table 2 Elastic modulus for Cr40 alloy steel at different temperatures [37]

T/°C	E/GPa
25	211
100	208
200	202
300	195
400	186

The effect of temperature gradient on the stress waves can be analytically investigated when the temperature distributions on the incident and transmitted bars are known. According to the one-dimensional stress wave theory, when a P-wave vertically incidents from medium 1 to medium 2, the relation of the incident stress (σ_i), reflected stress (σ_r) and transmitted stress (σ_t) will be written as

$$\begin{cases} \sigma_r = \dfrac{\rho_2 c_2 A_2 - \rho_1 c_1 A_1}{\rho_1 c_1 A_1 + \rho_2 c_2 A_2}\sigma_i \\ \sigma_t = \dfrac{2\rho_2 c_2 A_1}{\rho_1 c_1 A_1 + \rho_2 c_2 A_2}\sigma_i \end{cases} \tag{2}$$

where A_1 and A_2 are the cross-sectional area of media 1 and 2, respectively; ρ_1 and ρ_2 are the density of media 1 and 2, respectively; c_1 and c_2 are the P-wave velocity of media 1 and 2, respectively.

For the steel bars, it can be assumed that the density and cross-sectional area are constant. Thus, a simplified form of Eq. (2) is

$$\begin{cases} \sigma_r = \dfrac{c_2 - c_1}{c_1 + c_2}\sigma_i \\ \sigma_t = \dfrac{2c_2}{c_1 + c_2}\sigma_i \end{cases} \tag{3}$$

For Eq. (3), the value of c can be found from

$$c = \sqrt{E/\rho} \tag{4}$$

The best fit of elastic modulus and temperature is E=−0.00008T^2−0.03271T+211.92123, R^2=0.9998. Thus, Eqs. (3) and (4) can be used to calculate the stress waves on the bars if the bars are divided into several segments, as described in Fig. 7. In Fig. 7, the length of the element (l_i) is set according to the wave velocity (c_i) and the time interval (Δt), i.e., l_i=$c_i\Delta t$, where Δt is equal to the acquisition rate of oscilloscope [16]. Because the length of each element is divided based on the wave velocity of each segment, the time of wave to pass any element is both Δt.

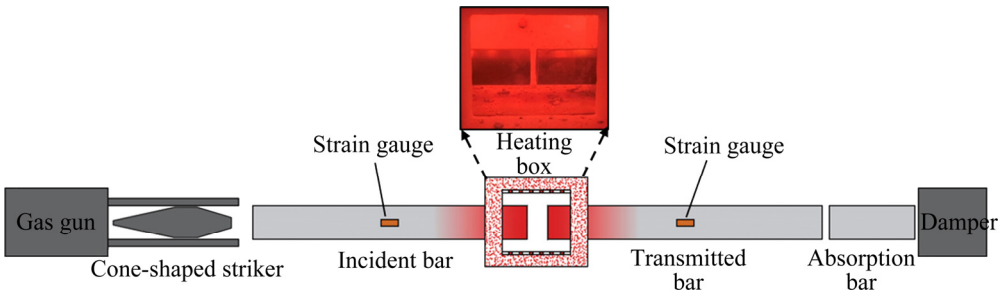

Fig. 4 Schematic diagram for testing effect of temperature gradient on incident waves

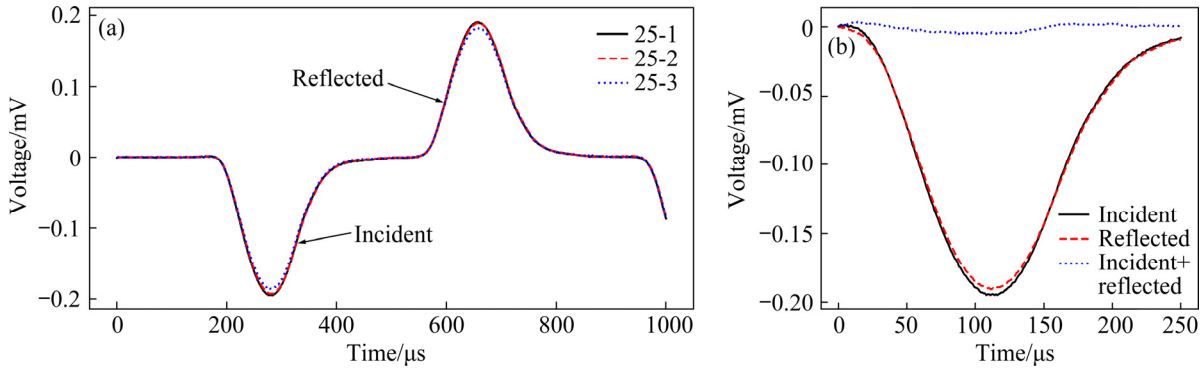

Fig. 5 Stress wave signals for Specimens 25-1, 25-2, and 25-3 (a), and comparison between incident and reflected waves for Specimen 25-1 (b)

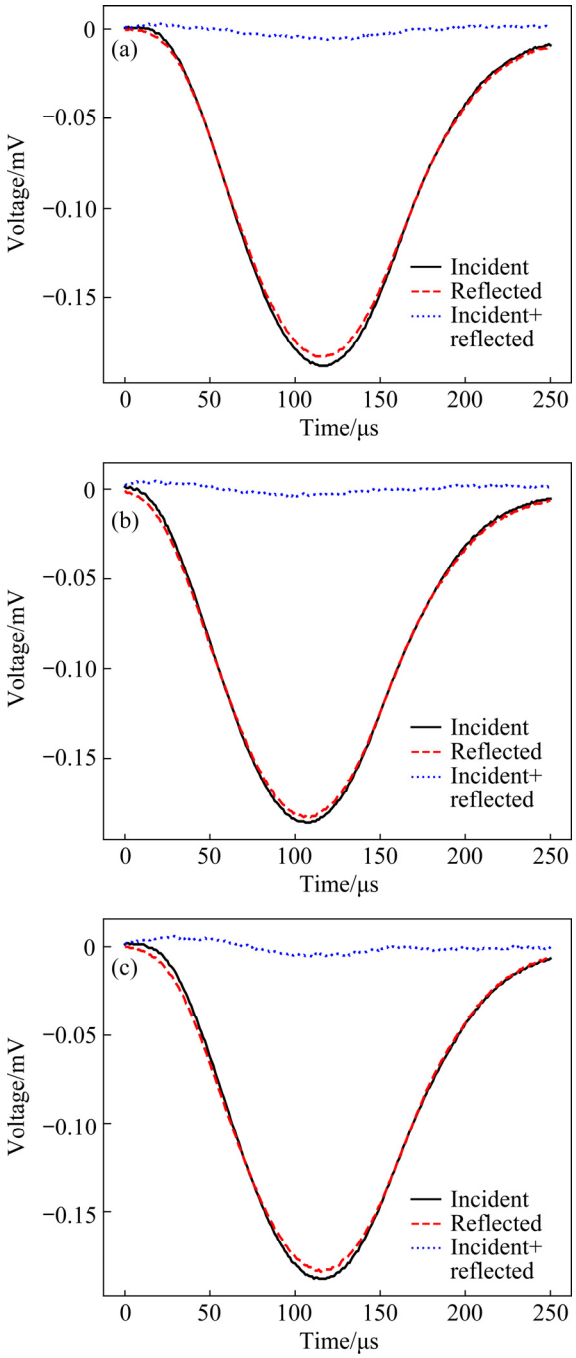

Fig. 6 Comparison between incident and reflected waves for 100 °C (a), 200 °C (b), and 400 °C (c)

Without loss of generality, it is supposed that there is a Cr40 steel bar, with a length of 4 m and a diameter of 50 mm, heated to a high temperature of 400 °C at its middle position, as shown in Fig. 8. The temperature distribution on the left and right parts was the same as the temperature distribution of the incident bar in Fig. 3, and the temperature distribution on its cross-section area was uniform. A half-sine stress wave (σ_i) was vertically incident to the bar from the left cross-section. We could observe the variation of the stress wave when it passes through measuring Points 1, 2, and 3. When it propagates from Point 1 to Point 2, it may describe the propagation of an incident wave from the normal temperature part to the high-temperature part of the bar. And, when it propagates from Point 2 to Point 3, it may describe the propagation of a transmitted (reflected) wave from the high-temperature part to the normal temperature part of the bar.

Figure 9(a) shows the stress histories collected from measuring Points 1, 2, and 3. The stress wave recorded at Point 1 can be regarded as the waveform that had not been affected by the temperature gradient. When the stress wave propagated from Point 1 to Point 2, a decrement in the amplitude of the stress wave is observed. This phenomenon is understandable because the elastic modulus of the bar would decrease with the increase in temperature. So, the actual stress waves on the right- and left-hand sides of the specimen should be less than those collected by the strain gauges. When the stress wave transmits from Point 2 to Point 3, we could observe that the amplitude of the stress wave increases again. The reason why the stress wave increases again is that, according to Eq. (3), the transmitted wave tends to increase when it propagates from the section with low P-wave velocity to the section with a higher P-wave velocity.

Figure 9(b) compares the stress waveforms recorded at measuring Points 1, 2, and 3. It can be observed that the temperature gradient on the bar only results in a slight decrement of the amplitude of the stress wave at Point 2, and the shape of the stress wave at Point 3 is less affected by the temperature gradient, which may help to discuss

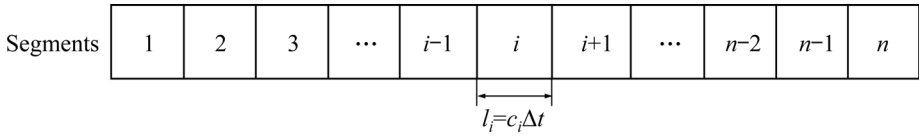

Fig. 7 Schematic diagram of element division of steel bar

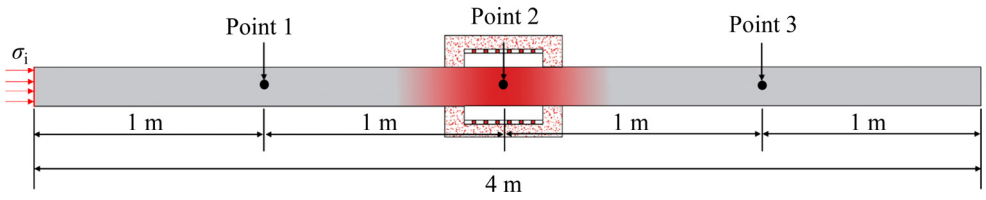

Fig. 8 Schematic diagram of Cr40 steel bar subjected to high temperature at its middle position

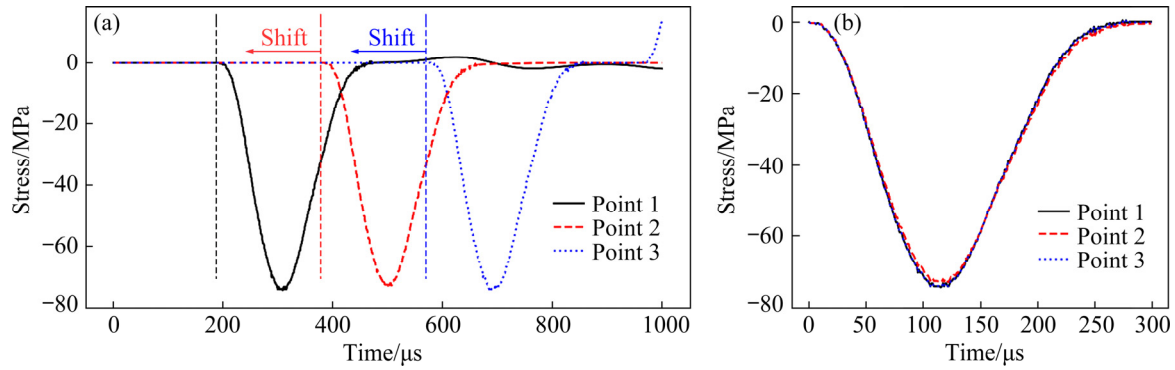

Fig. 9 Effect of time on stress waveform: (a) Wave history; (b) Comparison between stress waves at measuring Points 1, 2, and 3

why the reflected wave is insensitive to the high-temperature gradient. Significantly, it seems that the stress wave at Point 3 is entirely equal to that at Point 1. Although no distinct difference can be observed from the figure, the amplitude of the stress wave at Point 3 is 0.1% less than that at Point 1.

Therefore, based on the above analyses, we could estimate the stress wave at Point 2 through the stress wave at Point 1 or Point 3. It can be assumed that there is a relationship between the measured and the actual stress waves [16]:

$$\sigma_A=\lambda_T\sigma_M \tag{5}$$

where σ_M and σ_A are the measured and actual stress wave, respectively; λ_T is the temperature-dependent factor.

Figure 10 shows the comparison between the stress waveform obtained from measuring Point 2 and that calculated from Eq. (5), where the λ_T is set as 0.982. It can be seen that Eq. (5) is sufficiently precise to predict the stress waveform at high temperatures. The same analyses were conducted when supposing the steel bar was heated to 100 and 200 °C, respectively, and the obtained λ_T for 100 and 200 °C is 0.998 and 0.994, respectively. It should be noted that a similar procedure is also conducted by YIN et al [16] to correct the stress wave. However, they neglected the wave reflection

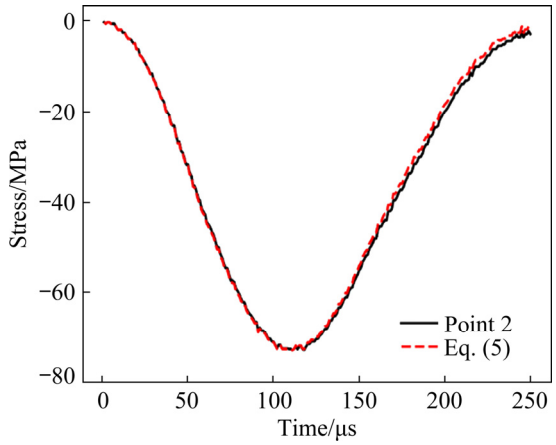

Fig. 10 Comparison of stress wave of measuring Point 2 and prediction of Eq. (5)

between the adjacent elements, which overestimates the effect of the temperature gradient on the stress waves. If the refection is neglected, in this work, the obtained correction factors are 0.996, 0.989, and 0.969 for 100, 200, and 400 °C, respectively, which is the same as the results obtained by YIN et al [16].

From the above analysis, we could notice that although the tests were performed at a high temperature of 400 °C, the effect of the temperature gradient on the stress wave is limited. For indoor tests, when the experiment temperature is less than or equal to 400 °C, we may estimate the forces on both sides of the specimen by substituting Eq. (5) into Eq. (1):

$$P_1^{\mathrm{R}}=\lambda_{\mathrm{T}}P_1,\ P_2^{\mathrm{R}}=\lambda_{\mathrm{T}}P_2 \tag{6}$$

where P_1^{R} is the actual force on the left hand of the specimen, and P_2^{R} is the actual force on the right hand of the specimen.

3.2 Dynamic force balance verification and calculation of dynamic fracture toughness

The dynamic force balance should be verified before the calculation of the dynamic fracture toughness. Figure 11(a) shows the signal history collected by the strain gauges on the incident and transmitted bars when an NSCB specimen is loaded at 400 °C. The time-zero of the incident reflected and transmitted forces are shifted into the right and left cross-section of the incident and transmitted bars, respectively. Figure 11(b) shows the typical force histories, where the forces are calculated based on Eq. (6). It can be seen from Fig. 11(b) that the dynamic force equilibrium is achieved when the specimen is at ambient high temperature of 400 °C. The result further manifests that the tests are valid. Therefore, the inertial effects are negligible, and the average dynamic load ($\bar{P}$) on the NSCB specimen can be expressed as

$$\bar{P}(t)=\frac{1}{2}[P_1^{\mathrm{R}}(t)+P_2^{\mathrm{R}}(t)]=P_1^{\mathrm{R}}(t)=P_2^{\mathrm{R}}(t) \tag{7}$$

The dynamic stress intensity factor (K_{I}) can be calculated on the quasi-static formula [35]:

$$K_{\mathrm{I}}(t)=\frac{\bar{P}(t)\sqrt{\pi a}}{2RB}Y_{\mathrm{I}} \tag{8}$$

where Y_{I} is the mode I normalized stress intensity factor for NSCB specimen as [35]

$$Y_{\mathrm{I}}=-1.297+9.516\beta+(-0.47-16.457\beta)\alpha+(1.071+34.401\beta)\alpha^2$$
$$(0.2\leq\alpha\leq0.6,\ 0.5\leq\beta\leq0.8) \tag{9}$$

and $\alpha=a/R$, $\beta=S/(2R)$.

Before the calculation of dynamic fracture toughness (K_{Id}), the fracture process of the NSCB specimen should be reviewed to verify the fracture mode of the specimen. The typical fracture process and the fracture surfaces of the NSCB specimens at different temperatures are shown in Fig. 12. From Fig. 12, the cracks initiate at the crack notch at 60−71 μs from the prefabricated notch for all temperature group specimens. And, after further 5 μs, the cracks almost entirely pass through the ligament of the specimens and divide the specimens into two identical parts. One can also notice the smooth fracture surfaces of the specimens, which strongly indicates that the mode I fracture occurs. The fracture behaviors are the same as the fracture characteristics of the NSCB specimen described in Ref. [38].

From the above analyses, the effectiveness of the fracture tests is verified and the dynamic fracture toughness and the loading rate of the specimens can be determined. Based on Eq. (8), the dynamic mode I stress intensity factor (SIF) history of the NSCB specimen can be derived, and a typical dynamic SIF history is shown in Fig. 13. According to the ISRM method [23], the loading rate ($\dot{K}_{\mathrm{I}}$) is obtained from the slope of the linear regime of the SIF−time curve, and the peak value of the curve is regarded as the dynamic fracture toughness (K_{Id}) of the NSCB specimen. It should be noted that some literature [39,40] indicated that the crack initiation time is not synchronized with the peak load. However, the cracks are found to nearly penetrate the specimens within 5 μs. The peak value of SIF occurs at 72 μs (Fig. 13), and even if the crack onset time is 67 μs, the peak SIF (9.17 MPa·m$^{0.5}$) is only 1.44% larger than that at 67 μs (9.04 MPa·m$^{0.5}$). Besides, in a numerical study, XU

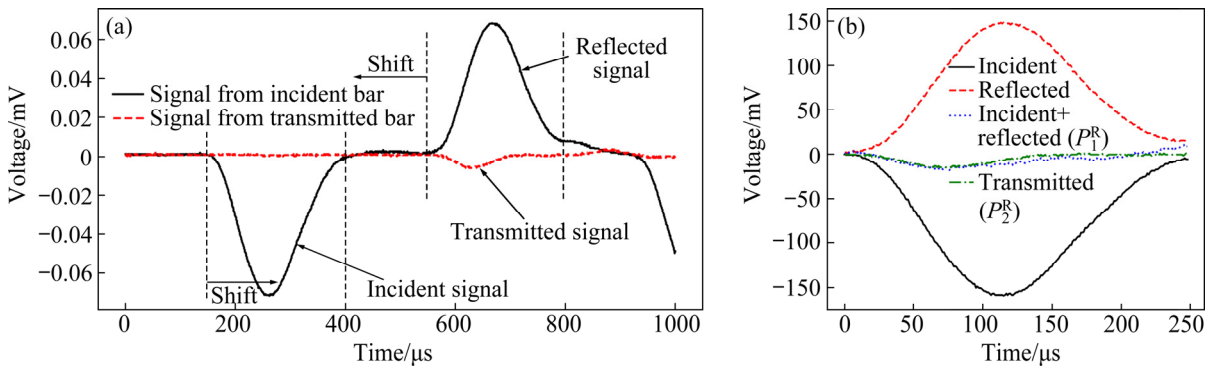

Fig. 11 Typical signal history (a) and dynamic force equilibrium (b) for test at 400 °C

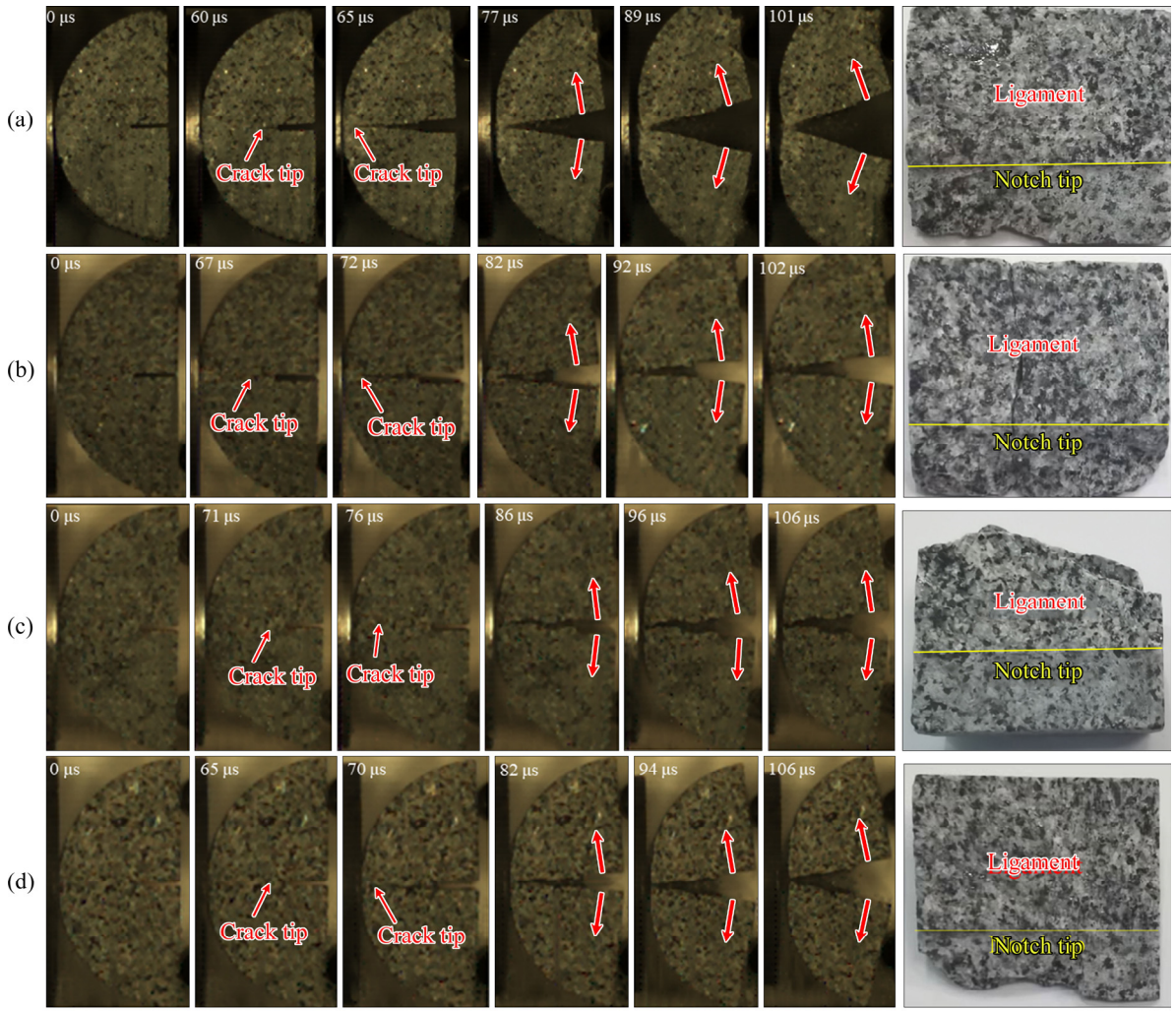

Fig. 12 Typical fracture photographs and fracture surfaces of dynamic NSCB tests at different temperatures: (a) T=25 °C; (b) T=100 °C; (c) T=200 °C; (d) T=400 °C

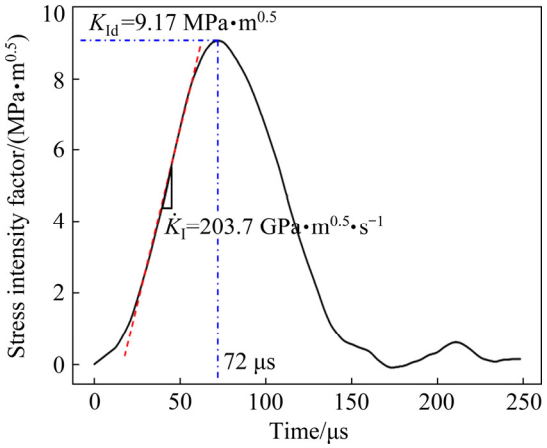

Fig. 13 Determination of dynamic fracture toughness and loading rate of NSCB specimen

et al [41] indicated that the time difference between the fracture onset and peak force is 4.62−5.95 μs, which demonstrates that the moment of crack initiation almost synchronizes with the peak force. Therefore, using the peak value of the SIF as the dynamic mode I fracture toughness would not profoundly overestimate the dynamic mode I fracture toughness. And, for all of the NSCB specimens, the dynamic force equilibrium and fracture mode are rigidly checked.

4 Results and discussion

The obtained dynamic fracture toughness and loading rates of NSCB specimens at different temperatures are shown in Table 3. The restored NSCB specimens after dynamic impact are shown in Fig. 14. The loading rates for these specimens were 199.3−254.6 GPa·m$^{0.5}$·s^{-1}. It can be observed

Table 3 Dynamic fracture toughness of NSCB specimens at different high temperatures

Specimen	$\dot{K}_I$ /(GPa·m$^{0.5}$·s^{-1})	K_I^d /(MPa·m$^{0.5}$)	Specimen	$\dot{K}_I$ /(GPa·m$^{0.5}$·s^{-1})	K_I^d /(MPa·m$^{0.5}$)
25-1	121.6	6.45	200-1	148.9	7.58
25-2	254.6	9.78	200-2	199.3	10.1
25-3	319.3	10.77	200-3	373.6	14.55
25-4	343.9	12.62	200-4	390.1	14.33
25-5	446.1	14.34	200-5	420.4	15.31
25-6	460.0	14.76	200-6	452.0	18.4
25-7	460.8	15.49	200-7	495.0	16.54
25-8	546.0	17.43	200-8	508.2	18.01
100-1	148.5	6.39	400-1	122.2	7.34
100-2	224.8	8.84	400-2	203.7	9.17
100-3	328.1	12.46	400-3	275.6	10.78
100-4	383.4	13.99	400-4	323.2	14.34
100-5	386.4	15.01	400-5	391.9	15.32
100-6	414.6	14.56	400-6	415.8	16.04
100-7	458.2	15.82	400-7	457.6	15.43
100-8	526.4	16.78	400-8	469.3	17.26

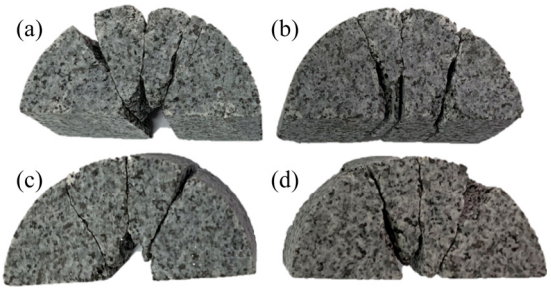

Fig. 14 Restored NSCB specimens after being subjected to dynamic impact at different temperatures: (a) Specimen 25-2, loading rate 254.6 GPa·m$^{0.5}$·s^{-1}; (b) Specimen 100-2, loading rate 224.8 GPa·m$^{0.5}$·s^{-1}; (c) Specimen 200-2, loading rate 199.3 GPa·m$^{0.5}$·s^{-1}; (d) Specimen 400-2, loading rate 203.7 GPa·m$^{0.5}$·s^{-1}

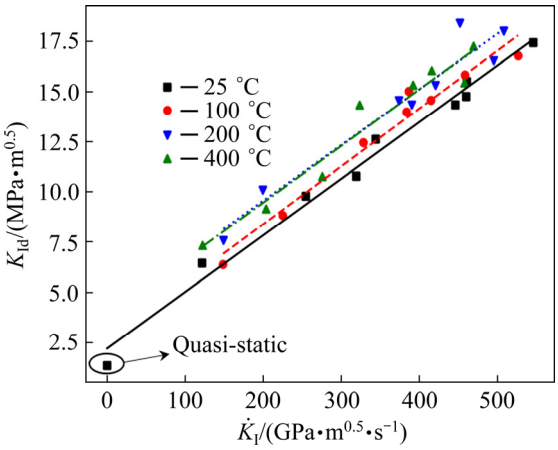

Fig. 15 Dynamic fracture toughness versus loading rate of Fujian granite at different temperatures

that there was no obvious difference whether the specimens were at 25 °C or 400 °C. The specimens were uniformly fractured into four pieces and the fracture patterns for the specimens were similar.

Figure 15 shows the variation of the dynamic fracture toughness and loading rate for NSCB specimens at different temperatures, where the quasi-static value is obtained from Ref. [32]. It can be seen from Fig. 15 that the dynamic fracture toughness increases linearly with the increase of loading rate. This phenomenon can also be found [42,43]. LI et al [42] carried out a dynamic study to test the mode I fracture properties of Barre granite after being subjected to microwave irradiation. They claimed that the dynamic fracture toughness increases linearly with the loading rate, and, although the microwave irradiation showed an obvious weakening effect on the fracture toughness under the same loading rate, the slopes of the regression curves are constant. YAO et al [43] conducted a series of dynamic fracture tests on two thermally treated mortar samples, and their results also pointed out that the dynamic fracture toughness linearly develops as the loading rate increases, and, under the same loading rate, the dynamic fracture

toughness decreased with an increase in heat-treatment temperature. They expressed that the decrement of dynamic fracture toughness under the same loading rate was due to the development of micro-cracks and voids at different temperature phases.

In this work, the experimental results indicate that the temperature has a strengthening effect on the dynamic fracture toughness of the granite, which is counter-intuitive because the thermal treatment would usually decrease the rock dynamic fracture toughness [44,45]. The quasi-static tests (such as those described in Refs. [46−49]) also showed the negative effects of thermal treatment on the fracture toughness of rocks. For this granite, the static mode I fracture toughness under natural conditions is 1.349 MPa·m$^{0.5}$ [32]. However, the mode I fracture toughness of this granite decreases to 0.935 MPa·m$^{0.5}$ when the temperature increases to 400 °C [32], which demonstrates that there exist essential differences between the rock properties after and at ambient high temperature.

The scanning electron microscope (SEM) images of the granite after being subjected to different temperatures are presented in Fig. 16. When the temperatures are 25 and 100 °C, no obvious thermal cracks are observed, which suggests that no thermal damages occur when the granite is heated to the 100 °C. When the temperature increases to 200 and 400 °C, apparent thermal cracks emerge, which demonstrates that the thermal damages occur in the temperature stages. However, the micrographs after high temperatures might not reflect the nature of rocks at ambient high temperature, because the thermal damages can occur in the heating stage or cooling stage or both depending on the rock types and temperature conditions [50−52]. For instance, DAOUD et al [52] investigated the AE characteristics of three intrusive igneous rocks during cyclic heating and cooling treatment, and the results indicated that thermal damage can occur at both the heating and cooling stages for Slaufrudalar Granophyre, but, for Santorini Andesite and Seljadalur Basalt, the thermal damage generates mainly at the cooling stage. Although the temperature could motivate the extension and the formation of microcracks, the high temperature could also motivate the evaporation of free water and the closure of primary cracks, which may both have certain positive effects on the rock strength. While, for the granite used in the study, the thermal damage might not have occurred yet even when the temperature reaches 400 °C. This is why the temperature shows

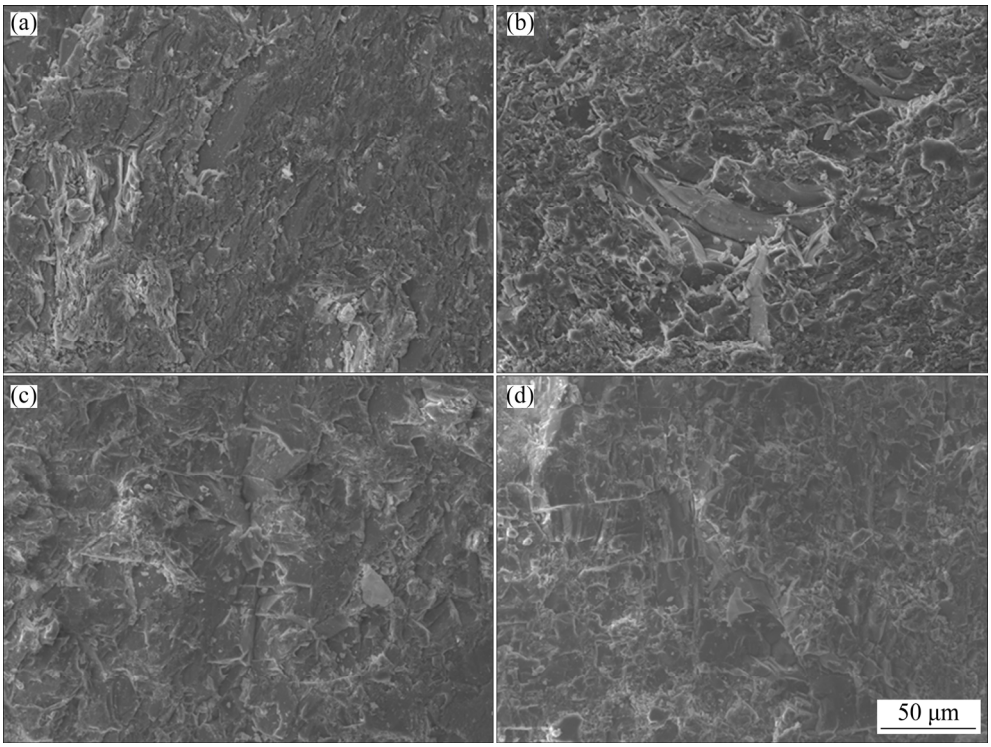

Fig. 16 Micro-photographs of specimens after being subjected to different temperatures: (a) 25 °C; (b) 100 °C; (c) 200 °C; (d) 400 °C

a strengthening effect on the dynamic fracture toughness.

However, the temperature may have both the strengthening effect and the weakening effect on the rock dynamics strength. LIU and XU [10] indicated that the temperature strengthens the dynamic compressive strength of sandstone in a temperature range of 25−400 °C. Whereas, when the temperature increases to over 400 °C, the temperature shows a weakening effect on the dynamic compressive strength. YIN et al [16] showed that the dynamic tensile strength of sandstone in the temperature range of 100−500 °C is higher than that at 25 °C under the same loading rate. However, the dynamic tensile strength of the sandstone at 600 °C is smaller than that at 25 °C under the same loading rate. PING et al [17] also indicated that the dynamic tensile strength of sandstone first increases within the temperature ranges of 25−400 °C and then decreases as the temperature further increases to 800 °C.

Thus, it can be concluded that there is a temperature threshold for rocks. When the temperature is lower than the threshold, the rock will be strengthened. However, when the temperature increases to over the threshold, the rock strength will be weakened. In the literature [10,16,17], the temperature threshold is in the temperature range of 400−600 °C. It is worth mentioning that the α−β phase transition of quartz occurs at around 573 °C [46,53]. The thermal effect on the dynamic properties of rocks at high temperatures will be reversed when the temperature exceeds this temperature point.

In this work, only the dynamic fracture toughness of granite at four temperature (25, 100, 200, and 400 °C) was tested. It is possible to carry out dynamic fracture tests when the temperature is higher than 400 °C. However, when the specimen is heated to over 400 °C, the steel bars may be tempered, and its elastic parameters may be permanently changed. Therefore, to prolong the service life of the system, the fracture tests were only conducted within the temperature ranges of 25−400 °C. However, considering that in an enhanced geothermal system (EGS), the hot dry rock at temperatures of 150−350 °C is high enough to generate power [54], the test results are still meaningful. Figure 17 shows the comparison between the test results presented in this study and the results obtained by ZHANG et al [18] and YIN et al [19]. From Fig. 17, it is observed that the dynamic fracture toughness depends mainly on the loading rate.

Many factors affect the variation of dynamic fracture toughness during the dynamic test. Different rocks may display different fracture behaviors at ambient high temperatures. And, different specimen sizes and geometries may yield different dynamic fracture toughness values [55−57]. Therefore, more dynamic fracture studies on different rock types, specimen sizes, and specimen geometries are still to be carried out in the future to verify the results presented in the text.

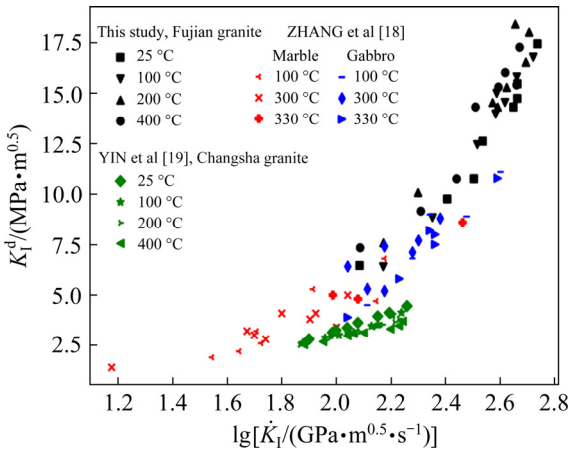

Fig. 17 Comparison between dynamic fracture toughness of different rocks at different temperatures

5 Conclusions

(1) Analytical results reveal that the amplitude of the stress wave decreases when it propagates from the normal temperature part to the high-temperature part of the bar. However, the stress wave will grow again when it further propagates from the high-temperature part to the room temperature part of the bar.

(2) Although the steel bars and the NSCB specimens are both at ambient high temperatures, the dynamic tests forces balance can be achieved, which further demonstrates that the test method is valid.

(3) The fracture tests show that the temperature has a strengthening effect on the dynamic fracture toughness for the granite, and the dynamic fracture toughness increases linearly within the loading rate of 121.6−546.0 GPa·m$^{0.5}$·s^{-1}.

(4) This work may have certain implications

for designing the high-temperature rock structures and the dynamic fracturing in hot dry rock. However, further research should be made on the different types of rocks and different types/sizes of specimens to verify the results drawn in the study.

Acknowledgments

The authors are very grateful for the financial support from the National Natural Science Foundation of China (No. 41972283). The authors also like to thank Mr. Deng-deng ZHUANG for his help with analyzing the scanning electron micro-photographs.

References

[1] GOMEZ-HERAS M, MCCABE S, SMITH B J, FORT R. Impacts of fire on stone-built heritage [J]. Journal of Architectural Conservation, 2009, 15: 47−58.

[2] WASANTHA P L P, GUERRIERI M, XU T. Effects of tunnel fires on the mechanical behaviour of rocks in the vicinity—A review [J]. Tunnelling and Underground Space Technology, 2021, 108: 103667.

[3] DEROSA M. Analysis of mine fires for all US metal/ nonmetal mining categories, 1990—2001 [M]. Pittsburgh, PA: National Institute for Occupational Safety and Health-NIOSH, 2004.

[4] LONG Yi, LIU Jian-po, LEI Gang, SI Ying-tao, ZHANG Chang-yin, WEI Deng-cheng, SHI Hong-xu. Progressive fracture processes around tunnel triggered by blast disturbances under biaxial compression with different lateral pressure coefficients [J]. Transactions of Nonferrous Metals Society of China, 2020, 30(9): 2518−2535.

[5] WANG Yun-jia, TIAN Feng, HUANG Yi, WANG Jian, WEI Chang-jing. Monitoring coal fires in Datong coalfield using multi-source remote sensing data [J]. Transactions of Nonferrous Metals Society of China, 2015, 25(10): 3421−3428.

[6] CARVEL R. Lessons learned from catastrophic fires in tunnels [J]. Civil Engineering, 2008, 161: 49−53.

[7] GUO Y D, HUANG L Q, LI X B, CHEN J Z, SUN J M. Experimental investigation on the effects of thermal treatment on the physical and mechanical properties of shale [J]. Journal of Natural Gas Science and Engineering, 2020, 82:103496.

[8] XIA J Q, DOU B, TIAN H, ZHENG J, CUI G, KASHIF M. Research on initiation of carbon dioxide fracturing pipe using the liquid carbon dioxide phase-transition blasting technology [J]. Energies, 2021, 14: 521.

[9] LIU S, XU J Y. Study on dynamic characteristics of marble under impact loading and high temperature [J]. International Journal of Rock Mechanics and Mining Sciences, 2013, 62: 51−58.

[10] LIU S, XU J Y. Effect of strain rate on the dynamic compressive mechanical behaviors of rock material subjected to high temperatures [J]. Mechanics of Materials, 2015, 82: 28−38.

[11] YIN Tu-bing, SHU Rong-hua, LI Xi-bing, WANG Pin, DONG Long-jun. Combined effects of temperature and axial pressure on dynamic mechanical properties of granite [J]. Transactions of Nonferrous Metals Society of China, 2016, 26(8): 2209−2219.

[12] WONG L N Y, LI Z, KANG H M, TEH C I. Dynamic loading of Carrara marble in a heated state [J]. Rock Mechanics and Rock Engineering, 2017, 50: 1487−1505.

[13] WANG Z L, SHI H, WANG J G. Mechanical behavior and damage constitutive model of granite under coupling of temperature and dynamic loading [J]. Rock Mechanics and Rock Engineering, 2018, 51: 3045−3059.

[14] PING Q, WU M J, YUAN P, ZHANG H. Experimental study on dynamic mechanical properties of high temperature sandstone under impact loads [J]. Chinese Journal of Mechanical Engineering, 2019, 38: 782−792. (in Chinese)

[15] YANG G L, LIU J, LI X G, BI J J. Effect of temperature on shale strength under dynamic impact loading [J]. Arabian Journal of Geosciences, 2020, 13: 1−9.

[16] YIN T B, WANG C, WU Y, WU B Q. A waveform modification method for testing dynamic properties of rock under high temperature [J]. Journal of Rock Mechanics and Geotechnical Engineering, 2021, 13: 833−844.

[17] PING Q, WU M J, YUAN P, SU H P, ZHANG H. Dynamic splitting experimental study on sandstone at actual high temperatures under different loading rates [J]. Shock and Vibration, 2020, 2020: 1−12.

[18] ZHANG Z X, YU J, KOU S Q, LINDQVIST P A. Effects of high temperatures on dynamic rock fracture [J]. International Journal of Rock Mechanics and Mining Sciences, 2001, 38: 211−225.

[19] YIN T B, ZHANG S S, LI X B, BAI L. A numerical estimate method of dynamic fracture initiation toughness of rock under high temperature [J]. Engineering Fracture Mechanics, 2018, 204: 87−102.

[20] ZHANG Z X, KOU S Q, YU J, YU Y, JIANG L G, LINDQVIST P A. Effects of loading rate on rock fracture [J]. International Journal of Rock Mechanics and Mining Sciences, 1999, 36: 597−611.

[21] ZHANG S, WANG Q Z. Method for determination of dynamic fracture toughness of rock using holed-cracked flattened disk specimen [J]. Chinese Journal of Mechanical Engineering, 2006, 28(6): 723−728. (in Chinese)

[22] NAKANO M, KISHIDA K, YAMAUCHI Y, SOGABE Y. Dynamic fracture initiation in brittle materials under combined mode I/II loading [J]. Le Journal De Physique IV, 1994, 4(C8): 695−700.

[23] ZHOU Y X, XIA K, LI X B, LI H B, MA G W, ZHAO J, ZHOU Z L, DAI F. Suggested methods for determining the dynamic strength parameters and mode-I fracture toughness of rock materials [J]. International Journal of Rock Mechanics and Mining Sciences, 2012, 49: 105−112.

[24] DAI F, XIA K W, ZHENG H, WANG Y X. Determination of dynamic rock Mode-I fracture parameters using cracked chevron notched semi-circular bend specimen [J]. Engineering Fracture Mechanics, 2011, 78: 2633−2644.

[25] YI Wei, RAO Qiu-hua, LI Zhuo, SHEN Qing-qing. A new measurement method of crack propagation rate for brittle rock under THMC coupling condition [J]. Transactions of

Nonferrous Metals Society of China, 2019, 29(8): 1728−1736.

[26] XIE Qin, LI Sheng-xiang, LIU Xi-ling, GONG Feng-qiang, LI Xi-bing. Effect of loading rate on fracture behaviors of shale under mode I loading [J]. Journal of Central South University, 2020, 27: 3118−3132.

[27] OH S W, MIN G J, PARK S W, KIM M S, OBARA Y, CHO S H. Anisotropic influence of fracture toughness on loading rate dependency for granitic rocks [J]. Engineering Fracture Mechanics, 2019, 221: 106677.

[28] BAHMANI A, FARAHMAND F, JANBAZ M R, DARBANDI A H, GHESMATI-KUCHEKI H, ALIHA M R M. On the comparison of two mixed-mode I+III fracture test specimens [J]. Engineering Fracture Mechanics, 2021, 241: 107434.

[29] BAHMANI A, ALIHA M R M, SARBIJAN M J, MOUSAVI S S. An extended edge-notched disc bend (ENDB) specimen for mixed-mode I+II fracture assessments [J]. International Journal of Solids and Structures, 2020, 193/194: 239−250.

[30] ALIHA M R M, AYATOLLAHI M R, AKBARDOOST J. Typical upper bound–lower bound mixed mode fracture resistance envelopes for rock material [J]. Rock Mechanics and Rock Engineering, 2012, 45: 65−74.

[31] TENG Ji-wen, SI Xiang, ZHUANG Qing-xiang, YAN Ya-fen, ZHENG Shuang-gao. Fine structures of crust and mantle and potential hot dry rock beneath the Zhangzhou Basin [J]. Chinese Journal of Geophysics, 2019, 62: 1613−1632. (in Chinese)

[32] YIN T B, WU Y, LI Q, WANG C, WU B Q. Determination of double-K fracture toughness parameters of thermally treated granite using notched semi-circular bending specimen [J]. Engineering Fracture Mechanics, 2020, 226: 106865.

[33] YIN T B, TAN X S, WU Y, YANG Z, LI M T. Temperature dependences and rate effects on Mode II fracture toughness determined by punch-through shear technique for granite [J]. Theoretical and Applied Fracture Mechanics, 2021, 114: 103029.

[34] WU Y, YIN T B, TAN X S, ZHUANG D D. Determination of the mixed mode I/II fracture characteristics of heat-treated granite specimens based on the extended finite element method [J]. Engineering Fracture Mechanics, 2021, 252: 107818.

[35] KURUPPU M D, OBARA Y, AYATOLLAHI M R, CHONG K P, FUNATSU T. ISRM-suggested method for determining the mode I static fracture toughness using semi-circular bend specimen [J]. Rock Mechanics and Rock Engineering, 2014, 47: 267−274.

[36] LI X B, LOK T S, ZHAO J. Dynamic characteristics of granite subjected to intermediate loading rate [J]. Rock Mechanics and Rock Engineering, 2005, 38: 21−39.

[37] The Engineering Materials Practical Manual Editorial Board. Practical manual for engeering materials [M]. 2nd ed. Beijing: China Standards Press, 2001. (in Chinese)

[38] CHEN R, XIA K, DAI F, LU F, LUO S N. Determination of dynamic fracture parameters using a semi-circular bend technique in split Hopkinson pressure bar testing [J]. Engineering Fracture Mechanics, 2009, 76: 1268−1276.

[39] ZHANG Q B, ZHAO J. Determination of mechanical properties and full-field strain measurements of rock material under dynamic loads [J]. International Journal of Rock Mechanics and Mining Sciences, 2013, 60: 423−439.

[40] DAI F, XU Y, ZHAO T, XU N W, LIU Y. Loading-rate-dependent progressive fracturing of cracked chevron-notched Brazilian disc specimens in split Hopkinson pressure bar tests [J]. International Journal of Rock Mechanics and Mining Sciences, 2016, 88: 49−60.

[41] XU Y, DAI F, XU N W, ZHAO T. Numerical investigation of dynamic rock fracture toughness determination using a semi-circular bend specimen in split Hopkinson pressure bar testing [J]. Rock Mechanics and Rock Engineering, 2016, 49: 731−745.

[42] LI X, WANG S, XU Y, YAO W, XIA K W, LU G M. Effect of microwave irradiation on dynamic mode-I fracture parameters of Barre granite [J]. Engineering Fracture Mechanics, 2020, 224: 106748.

[43] YAO W, XU Y, LIU H W, XIA K W. Quantification of thermally induced damage and its effect on dynamic fracture toughness of two mortars [J]. Engineering Fracture Mechanics, 2017, 169: 74−88.

[44] YIN T B, LI X B, XIA K W, HUANG S. Effect of thermal treatment on the dynamic fracture toughness of Laurentian granite [J]. Rock Mechanics and Rock Engineering, 2012, 45: 1087−1094.

[45] YIN T B, BAI L, LI X, LI X B, ZHANG S S. Effect of thermal treatment on the mode I fracture toughness of granite under dynamic and static coupling load [J]. Engineering Fracture Mechanics, 2018, 199: 143−158.

[46] NASSERI M H B, SCHUBNEL A, YOUNG R P. Coupled evolutions of fracture toughness and elastic wave velocities at high crack density in thermally treated Westerly granite [J]. International Journal of Rock Mechanics and Mining Sciences, 2007, 44: 601−616.

[47] ZUO J P, WANG J T, SUN Y J, CHEN Y, JIANG G H, LI Y H. Effects of thermal treatment on fracture characteristics of granite from Beishan, a possible high-level radioactive waste disposal site in China [J]. Engineering Fracture Mechanics, 2017, 182: 425−437.

[48] PENG K, LV H, YAN F Z, ZOU Q L, SONG X, LIU Z P. Effects of temperature on mechanical properties of granite under different fracture modes [J]. Engineering Fracture Mechanics, 2020, 226: 106838.

[49] GUO Q Z, SU H J, LIU J W, YIN Q, JING H W, YU L Y. An experimental study on the fracture behaviors of marble specimens subjected to high temperature treatment [J]. Engineering Fracture Mechanics, 2020, 225: 106862.

[50] ATKINSON B K, MACDONALD D, MEREDITH P. Acoustic response and fracture mechanics of granite subjected to thermal and stress cycling experiments [J]. Ser Rock Soil Mech, 1984, 8.

[51] BROWNING J, MEREDITH P, GUDMUNDSSON A. Cooling dominated cracking in thermally stressed volcanic rocks [J]. Geophysical Research Letters, 2016, 43: 8417−8425.

[52] DAOUD A, BROWNING J, MEREDITH P G, MITCHELL T M. Microstructural controls on thermal crack damage and the presence of a temperature-memory effect during cyclic thermal stressing of rocks [J]. Geophysical Research Letters, 2020, 47: e2020GL088693.

[53] HEUZE F E. High-temperature mechanical, physical and Thermal properties of granitic rocks — A review [J]. International Journal of Rock Mechanics and Mining Sciences & Geomechanics Abstracts, 1983, 20: 3−10.
[54] AVANTHI ISAKA B L, RANJITH P G, RATHNAWEERA T D. The use of super-critical carbon dioxide as the working fluid in enhanced geothermal systems (EGSs): A review study [J]. Sustainable Energy Technologies and Assessments, 2019, 36: 100547.
[55] ALIHA M R M, SISTANINIA M, SMITH D J, PAVIER M J, AYATOLLAHI M R. Geometry effects and statistical analysis of mode I fracture in guiting limestone [J]. International Journal of Rock Mechanics and Mining Sciences, 2012, 51: 128−135.
[56] AKBARDOOST J, AYATOLLAHI M R, ALIHA M R M, PAVIER M J, SMITH D J. Size-dependent fracture behavior of Guiting limestone under mixed mode loading [J]. International Journal of Rock Mechanics and Mining Sciences, 2014, 71: 369−380.
[57] ALIHA M R M, MAHDAVI E, AYATOLLAHI M R. Statistical analysis of rock fracture toughness data obtained from different chevron notched and straight cracked mode I specimens [J]. Rock Mechanics and Rock Engineering, 2018, 51: 2095−2114.

利用中心直裂纹半圆盘试样测定岩石在高温条件下的动态 I 型断裂韧度

吴 攸，尹土兵，刘希灵，谭小松，杨 政，李 樯

中南大学 资源与安全工程学院，长沙 410083

摘 要：为研究加载速率和高温对岩石动态断裂韧性的影响，利用分离式霍普金斯压杆对 4 种温度状态下的中心直裂纹半圆盘试样进行动态断裂试验。采用试验和解析方法研究杆中温度梯度对应力波的影响，并利用高速摄像机观察试样的破坏特征。结果表明：杆上的温度梯度不会使应力波的波形发生明显的变形；即使在 400 ℃条件下，试样也能达到应力平衡。在 25~400 ℃的温度条件下，岩石动态断裂韧度随着加载率的增加线性增长，且高温对岩石断裂韧度具有强化作用。

关键词：实时高温条件；动态断裂韧度；直裂纹半圆盘试样；分离式霍普金森压杆；福建花岗岩

(Edited by Xiang-qun LI)